



Cite this: *Nanoscale*, 2021, **13**, 17504

## Dual-site electrocatalytic nitrate reduction to ammonia on oxygen vacancy-enriched and Pd-decorated $\text{MnO}_2$ nanosheets<sup>†</sup>

Yan Wang,<sup>‡,a</sup> Song Shu,<sup>‡,b</sup> Min Peng,<sup>a</sup> Lin Hu,<sup>a</sup> Xiaoshu Lv,<sup>a</sup> Yu Shen,<sup>a</sup> Haifeng Gong<sup>a</sup> and Guangming Jiang<sup>ID, \*</sup><sup>a</sup>

Elecrocatalytic nitrate reduction (NRR) represents one promising alternative to the Haber–Bosch process for  $\text{NH}_3$  production due to the lower reaction energy barrier compared to  $\text{N}_2$  reduction and the potential recycling of nitrogen source from nitrate wastewater. The metal oxides with oxygen vacancy ( $\text{O}_v$ ) display high  $\text{NH}_3$  selectivities in NRR ( $\text{NO}_2^-/\text{N}_2$  as side products), but the complexity in  $\text{O}_v$  enrichment and the inferior hydrogen adsorption on oxides make NRR an inefficient process. Herein, one superior dual-site NRR catalyst that is composed of  $\text{O}_v$ -enriched  $\text{MnO}_2$  nanosheets ( $\text{MnO}_2\text{-O}_v$ ) and Pd nanoparticles (deposited on  $\text{MnO}_2$ ) is constructed over the three-dimensional porous nickel foam (Pd– $\text{MnO}_2\text{-O}_v/\text{Ni}$  foam). In a continuous-flow reaction cell, this electrode delivers a  $\text{NO}_3^-$ – $\text{N}$  conversion rate of  $642 \text{ mg N m}^{-2}\text{ electrode h}^{-1}$  and a  $\text{NH}_3$  selectivity of 87.64% at  $-0.85 \text{ V}$  vs.  $\text{Ag}/\text{AgCl}$  when feeding  $22.5 \text{ mg L}^{-1}$  of  $\text{NO}_3^-$ – $\text{N}$  ( $0.875 \text{ mL min}^{-1}$ ), outperforming the Pd/Ni foam ( $369 \text{ mg N m}^{-2}\text{ electrode h}^{-1}$ , 85.02%) and  $\text{MnO}_2\text{-O}_v/\text{Ni}$  foam ( $118 \text{ mg N m}^{-2}\text{ electrode h}^{-1}$ , 32.25%). Increasing the feeding  $\text{NO}_3^-$ – $\text{N}$  concentration and flow rate to  $180.0 \text{ mg L}^{-1}$  and  $2.81 \text{ mL min}^{-1}$  can further lift the conversion rate to 1933 and  $1171 \text{ mg N m}^{-2}\text{ electrode h}^{-1}$ , respectively. The combination of experimental characterizations and theoretical calculations reveal that the  $\text{MnO}_2\text{-O}_v$  adsorbs, immobilizes, and activates the  $\text{NO}_3^-$  and  $\text{N}$ -intermediates, while the Pd supplies the  $\text{O}_v$  sites with sufficient adsorbed hydrogen ( $\text{H}^+$ ) for both the NRR and  $\text{O}_v$  refreshment. Our work presents a good example of utilizing dual-site catalysis in the highly selective conversion of  $\text{NO}_3^-$  to  $\text{NH}_3$  that is important for nitrate pollution abatement, nitrogen resource recycling, as well as sustainable  $\text{NH}_3$  production.

Received 30th July 2021,  
Accepted 1st October 2021

DOI: 10.1039/d1nr04962c  
[rsc.li/nanoscale](http://rsc.li/nanoscale)

## 1. Introduction

Ammonia ( $\text{NH}_3$ ) is one important raw chemical with huge demand in the fertilizer, polymer, pharmaceutical, and explosive industries.<sup>1</sup> It is also a carbon-free hydrogen carrier that shows promise as a substituent for  $\text{H}_2$  fuel in the upcoming renewable energy era.<sup>2</sup> Currently, the industrial production of  $\text{NH}_3$  relies on the Haber–Bosch process that proceeds by the reaction of  $\text{N}_2$  and  $\text{H}_2$  under high temperatures ( $500 \text{ }^\circ\text{C}$ ) and pressures ( $>150 \text{ bar}$ ).<sup>3</sup> Albeit the considerable yield, this process with the harsh reaction condition is considered to be unsustainable in the context of energy saving and environ-

mental protection. Photo-/electrocatalytic  $\text{N}_2$  fixation with  $\text{H}_2\text{O}$  as the hydrogen source offers a green and sustainable way for  $\text{NH}_3$  production, but the yield is far from satisfying due to the chemical inertness of  $\text{N}_2$  (the triple bond energy reaches  $940.95 \text{ kJ mol}^{-1}$ ).<sup>4–6</sup> Recently, a novel route for  $\text{NH}_3$  production by electrocatalytic nitrate reduction (NRR) is proposed.<sup>7,8</sup> This route is considered promising as (i) the nitrate reduction to  $\text{NH}_3$  is more energy-efficient compared to  $\text{N}_2$  reduction,<sup>9</sup> and (ii) potential recycling of the nitrogen source from environmental pollutants, such as the  $\text{NO}_x$  (one gaseous pollutant that can be readily oxidized to nitrate)<sup>6</sup> and nitrite/nitrate in wastewater.<sup>10–12</sup> The catalyst is the core of the NRR system, determining both the kinetics and the product selectivity towards  $\text{NH}_3$  rather than  $\text{NO}_2^-$ ,  $\text{N}_2$ , or  $\text{N}_2\text{O}$ .<sup>13,14</sup> Among the tested catalysts, the transition metal oxides (such as  $\text{CuO}$ ,  $\text{FeO}_x$ , and  $\text{TiO}_2$ ) are gaining intensive attention due to their impressive NRR performances.<sup>15–17</sup> Some researchers evidenced that these oxides were partially reduced during NRR, forming oxygen vacancies ( $\text{O}_v$ ) at the surface coupled with the low-valent metal ions (e.g.  $\text{Cu}^+$  in  $\text{CuO-O}_v$ ,  $\text{Ti}^{3+}$  in  $\text{TiO}_2\text{-O}_v$ ).<sup>15,16</sup> They then proposed from theoretical calculations that  $\text{NO}_3^-$  was highly inclined to be harvested

<sup>a</sup>Engineering Research Center for Waste Oil Recovery Technology and Equipment, Ministry of Education, Chongqing Technology and Business University, Chongqing 400067, China. E-mail: [jiangguangming@zju.edu.cn](mailto:jiangguangming@zju.edu.cn)

<sup>b</sup>College of Architecture and Environment, Sichuan University, Chengdu 610065, China

†Electronic supplementary information (ESI) available. See DOI: [10.1039/d1nr04962c](https://doi.org/10.1039/d1nr04962c)

‡These two authors contribute equally to this work.

and immobilized at the  $O_v$  site with its oxygen atom filling in the vacancy, which restrained the migration of N-intermediates and their coupling to form  $N_2$  or  $N_2O$ . Furthermore, such an adsorption model enabled the activation of N–O bonds, promoting  $NO_3^-$  conversion.<sup>18</sup>

Albeit the unique role of  $O_v$  in NRR has been unveiled, its function is far from being fully exploited. Two aspects can be further improved: (i)  $O_v$  enrichment in the oxide ( $MO_x$ ). The formation of  $O_v$  requires the metal M of two or more oxidative valences (e.g.,  $Ti^{3+}/Ti^{4+}$  in  $TiO_2-O_v$  and  $Cu^{+}/Cu^{2+}$  in  $CuO-O_v$ ). In general,  $O_v$  in  $MO_x$  can be readily enriched when M binds with more oxygen (*i.e.*, a larger value of  $x$ ) in the initial fine oxide, owns more accessible oxidative valences, and can be reduced to the low valence under the NRR conditions.<sup>19,20</sup> The Mn in  $MnO_2$  has a valence of +4, and can be readily reduced to +2/+3 due to the corresponding positive redox potential (Table S1†). In this case, we believe more  $O_v$  can be readily formed in  $MnO_2$ , and the resultant  $MnO_2-O_v$  is expected to afford a better NRR performance.<sup>21</sup> (ii) Sufficient supply of hydrogen ( $H^*$ ) for NRR and  $O_v$  refreshment. The  $NH_3$  formation requires the  $H^*$  to combine with N-intermediates, while the  $O_v$  refreshment also requires the  $H^*$  to remove the oxygen/nitrogen species that fill the  $O_v$  during NRR. In general, the oxide is inferior in  $H^*$  adsorption,<sup>22,23</sup> and a more negative potential has to be employed to polarize the catalyst, which not only raises the energy consumption but also challenges the electrode stability (e.g.,  $-1.3$  V *vs.* SCE for  $FeNiO_x-O_v$ <sup>15</sup> and  $-1.6$  V *vs.* SCE for  $TiO_2-O_v$ <sup>17</sup>). The metallic palladium (Pd) is known as an excellent material for H adsorption.<sup>24,25</sup> We, therefore, propose that the coupling of the oxygen-deficient oxide and Pd can perform as one robust dual-site NRR electrocatalyst with high  $NH_3$  selectivity, in which the  $O_v$  serves to harvest, immobilize, and activate the  $NO_3^-$ , while the Pd supplies the  $O_v$  site with sufficient  $H^*$  from the aqueous solution. The dual-site catalysis has collected much success in heterogeneous catalytic reaction, but never reported in NRR.<sup>26–28</sup>

To confirm our hypothesis, a novel dual-site electrocatalyst that is composed of  $O_v$ -enriched  $MnO_2$  nanosheets ( $MnO_2-O_v$ ) and Pd nanoparticles (deposited on  $MnO_2$ ) was constructed over the three-dimensional porous nickel foam (Pd– $MnO_2-O_v$ /Ni foam). Its NRR performances, including the  $NO_3^-$ –N conversion rate,  $NH_3$ –N selectivity, and faradaic current efficiency, were tested in a continuous flow reactor and compared with those of Pd/Ni foam and  $MnO_2-O_v$ /Ni foam. Impacts of the  $NO_3^-$ –N feeding concentration, flow rate, solution pH, Pd loading mass, coexisting anions, and dissolved organic organisms on the NRR performances of Pd– $MnO_2-O_v$ /Ni foam were also investigated. Finally, how the dual sites work in the selective conversion of  $NO_3^-$  to  $NH_3$  is discussed with the aid of density functional theory (DFT) calculations.

## 2. Experimental methods

### 2.1. Materials

Analytical grade sodium nitrate ( $NaNO_3$ ), sodium nitrite ( $NaNO_2$ ), sodium sulfate ( $Na_2SO_4$ ), ammonium sulfate

( $(NH_4)_2SO_4$ ), anhydrous ethanol, sodium chloride ( $NaCl$ ), humic acid, sodium hydroxide, hydrochloric acid, titanium trichloride ( $TiCl_3$ ), potassium bromide ( $KBr$ ), potassium bromate ( $KBrO_3$ ), sulfamic acid ( $NH_2SO_3H$ ), sodium carbonate ( $Na_2CO_3$ ), sodium tetrachloropalladium ( $Na_2PdCl_4$ ), sodium sulfite ( $Na_2SO_3$ ), and potassium permanganate ( $KMnO_4$ ) were obtained from the Sinopharm group chemical reagent Co., Ltd, China. The 3D porous Ni foam substrate (110 pores per linear inch, surface density: 380 g m<sup>-2</sup>, thickness: 0.5 mm) was provided by Kunshan Tengerhui Electronic Technology Co., Ltd, China.

### 2.2. Synthesis of the electrode

For the synthesis of Pd– $MnO_2-O_v$ /Ni foam electrode, a Ni foam piece with a size of 35 mm × 35 mm × 0.5 mm and pre-cleaned by ethanol was placed in a Teflon-lined stainless-steel autoclave that contains 40 mL of  $KMnO_4$  aqueous solution (1.5 mM). The mixture was kept in an oven at 160 °C for 24 h to induce the growth of  $MnO_2$  on the Ni foam. Once being washed with deionized water at room temperature, the as-prepared  $MnO_2$ /Ni foam was subjected to a reduction current (−8.0 mA) in 10 mM of  $NaCl$  solution for 20 min to enrich the  $O_v$  on  $MnO_2$  ( $MnO_2-O_v$ /Ni foam), and the plotting of working potential *versus* reduction time can be seen in Fig. S1†. The as-synthesized  $MnO_2-O_v$ /Ni foam was then immediately immersed in a  $Na_2PdCl_4$  solution (1.0 mM, 100 mL) for 4.0 h to deposit Pd on the  $MnO_2-O_v$  sheet. In comparison, the cleaned Ni foam with pre-reduction at −8.0 mA for 20 min was immersed in  $Na_2PdCl_4$  solution (1.0 mM, 100 mL) for 4.0 h to produce the Pd/Ni foam.

### 2.3. NRR test

A sealed continuous-flow reaction cell with separated cathode and anode chambers by a cation-exchange membrane was customized for the NRR test. Two working electrodes (32 mm in diameter) were placed in the cathode chamber with a distance of 1.0 cm, and their working potentials were referred to the same Ag/AgCl wire (3.0 M KCl, 0.201 V *vs.* standard hydrogen electrode at 25 °C). One Pt foil was placed in the anode chamber as the counter electrode. The argon-saturated influent with 50 mM of  $Na_2SO_4$  and a certain amount of  $NO_3^-$ –N was pumped to the cathode chamber, and the NRR occurred when the effluent penetrated the working electrode. The feed in the anode chamber was only the argon-saturated 50 mM  $Na_2SO_4$  solution, and the oxygen evolution reaction occurred on the Pt foil. The concentrations (mg N mL<sup>-1</sup>) of  $NO_3^-$ –N ( $C_{NO_3^-}$ ),  $NO_2^-$ –N ( $C_{NO_2^-}$ ), and  $NH_3$ –N ( $C_{NH_3}$ ) in the inlet and outlet flow of the cathode chamber were quantified to calculate the  $NO_3^-$ –N conversion efficiency ( $\eta$ , 100%) and rate ( $r$ , mg N m<sup>-2</sup> electrode h<sup>-1</sup>), the product distribution (the decreased total N mass in solution after NRR is attributed to the escape of N in terms of  $N_2$ <sup>15,29</sup>),  $NH_3$ –N selectivity ( $S_{NH_3}$ , 100%), and the faradaic current efficiency (FE%, 100%):

$$\eta_{NO_3^-} = (C_{in,NO_3^-} - C_{out,NO_3^-})/C_{in,NO_3^-} \times 100\% \quad (1)$$

$$r_{NO_3^-} = (C_{in,NO_3^-} - C_{out,NO_3^-}) \times Q/A \times 60 \quad (2)$$

$$S_{\text{NH}_3^-} = C_{\text{out}, \text{NH}_3-\text{N}} / (C_{\text{in}, \text{NO}_3^--\text{N}} - C_{\text{out}, \text{NO}_3^--\text{N}}) \times 100 \quad (3)$$

$$\text{FE\%} = (n_1 \times C_{\text{out}, \text{NO}_2^--\text{N}} + n_2 \times C_{\text{out}, \text{NH}_3-\text{N}} + n_3 \times C_{\text{out}, \text{N}_2-\text{N}}) \times Q \times F / (M \times I) \times 10 \quad (4)$$

$$C_{\text{out}, \text{N}_2-\text{N}} = (C_{\text{in}, \text{NO}_3^--\text{N}} - C_{\text{out}, \text{NO}_3^--\text{N}} - C_{\text{out}, \text{NO}_2^--\text{N}} - C_{\text{out}, \text{NH}_3-\text{N}}) / 2 \quad (5)$$

where  $Q$ ,  $F$ ,  $M$ ,  $A$ , and  $I$  refer to the flowing rate of the influent ( $\text{mL min}^{-1}$ ), Faraday constant ( $96\,500 \text{ C mol}^{-1}$ ), molar mass of the element N ( $14\,000 \text{ mg mol}^{-1}$ ), geometric surface area of the electrode ( $\text{m}^2$ ), and current (A), respectively.  $n$  refers to the number of electrons transferred in the conversion of  $\text{NO}_3^--\text{N}$  to the corresponding nitrogen species (2, 5, and 8 for  $\text{NO}_2^--\text{N}$ ,  $\text{N}_2-\text{N}$ , and  $\text{NH}_3-\text{N}$ , respectively).

#### 2.4. DFT calculation

Spin-polarized density functional theory (DFT) calculations were carried out by the Perdew–Burke–Ernzerhof (PBE) functional within generalized gradient approximation (GGA), using the Vienna *ab initio* Simulation Package (VASP 5.4.1).<sup>30–32</sup> The kinetic energy cut off was set at 400 eV. The (111) facet-terminated  $2 \times 2$  supercell containing 48 Pd atoms and the (001) facet-terminated supercell containing 136 atoms (including 32 Mn, 76 O, 4 K, and 24 H) were constructed to model Pd and  $\delta\text{-MnO}_2$ , respectively. One oxygen atom was removed from the outermost layer of the  $\delta\text{-MnO}_2$  (001) facet to generate  $\text{MnO}_2-\text{O}_v$ . The vacuum space along the  $z$  direction was set to 15 Å, avoiding the interactions between two slab models. One layer at the bottom was fixed at the lattice position, while the remaining atomic layers and the absorbed molecules were fully relaxed. Brillouin zone integrations were performed using Monkhorst–Pack grids of  $3 \times 3 \times 1$  for all the slab calculations with Gaussian smearing  $\sigma = 0.1 \text{ eV}$ . All the structural optimizations were converged at  $0.05 \text{ eV \AA}^{-1}$ . The solvation effect was precluded since the ignorable energy change was witnessed.<sup>33,34</sup> Grimme's DFT-D3 method was incorporated to implement the van der Waals correction.<sup>35</sup>

The adsorption energy ( $E_{\text{ads}}$ ) is defined as

$$E_{\text{ads}} = E_{\text{tot}} - (E_{\text{sub}} + E_{\text{mol}}) \quad (6)$$

where  $E_{\text{tot}}$ ,  $E_{\text{sub}}$ , and  $E_{\text{mol}}$  depict the total energy of the adsorption complex, the substrate, and the isolated adsorbed molecules, respectively.

The free energies in the electrochemical reaction pathways were calculated based on the computational hydrogen electrode (CHE) model proposed by Nørskov and co-workers. The change in the Gibbs free energy ( $\Delta G$ ) for each reaction step is given as follows:<sup>36</sup>

$$\Delta G = \Delta E + \Delta ZPE - T\Delta S + \Delta U + \Delta pH \quad (7)$$

where  $\Delta E$  is the energy change between the reactant and product obtained from DFT calculations.  $\Delta ZPE$  is the change in zero-point energy, and  $T$  and  $\Delta S$  denote the temperature and change of entropy, respectively. Here,  $T = 298 \text{ K}$  was considered.  $\Delta pH$  is the free energy correction of pH, calculated by

$\Delta pH = kT \ln 10 \times \text{pH}$ , and the pH value is zero in this work. Additionally, the Gibbs free-energy diagrams were estimated under zero potential ( $U = 0$ ).

## 3. Results and discussion

### 3.1. Synthesis and characterization of the Pd–MnO<sub>2</sub>–O<sub>v</sub>/Ni foam electrode

The Pd/MnO<sub>2</sub>–O<sub>v</sub> nanosheets grown on the 3D-porous Ni foam were synthesized *via* a three-step approach: (i) growth of the uniform MnO<sub>2</sub> sheet array on the skeleton of Ni foam (MnO<sub>2</sub>/Ni foam); (ii) enrichment of O<sub>v</sub> on MnO<sub>2</sub> nanosheets *via* an electrochemical reduction method (MnO<sub>2</sub>–O<sub>v</sub>/Ni foam); (iii) further decoration of Pd NPs (Pd–MnO<sub>2</sub>–O<sub>v</sub>/Ni foam). Fig. 1a–d present the representative SEM images of Ni foam, MnO<sub>2</sub>/Ni foam, MnO<sub>2</sub>–O<sub>v</sub>/Ni foam, and Pd–MnO<sub>2</sub>–O<sub>v</sub>/Ni foam. As observed, MnO<sub>2</sub> grows on the smooth skeleton surface of Ni foam and displays a unique intersecting ribbon-like sheet structure. This structure is well preserved during the O<sub>v</sub> construction and Pd NP decoration. The Pd NPs are evenly deposited at the sheet surface with little agglomeration. The EDS elemental mapping results in Fig. 1e further demonstrate the even distribution of Pd, Mn, O, and Ni on the skeleton of Ni foam. In Fig. 1f, the HRTEM image of the Pd–MnO<sub>2</sub>–O<sub>v</sub> sheet

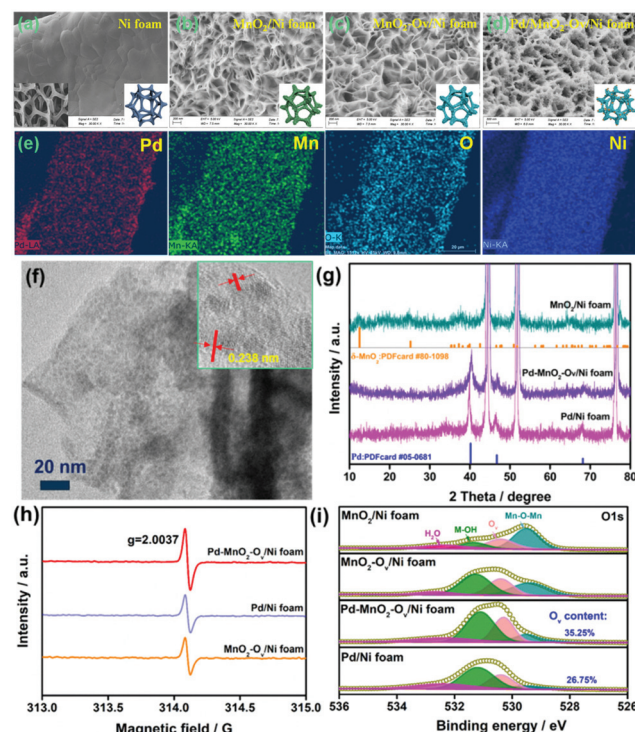


Fig. 1 Representative SEM images of (a) Ni foam, (b) MnO<sub>2</sub>/Ni foam, (c) MnO<sub>2</sub>–O<sub>v</sub>/Ni foam, and (d) Pd–MnO<sub>2</sub>–O<sub>v</sub>/Ni foam; (e) EDS elemental mapping of Pd, Mn, O, and Ni for Pd–MnO<sub>2</sub>–O<sub>v</sub>/Ni foam; (f) TEM image of Pd–MnO<sub>2</sub>–O<sub>v</sub> nanosheet (inset is the corresponding HRTEM image); (g) XRD patterns of electrodes; (h) EPR spectra and (i) high-resolution O 1s XPS spectra for different electrodes.

that is scraped from the Ni foam further evidences the intense and even deposition of Pd NPs with a mean size of 1.4 nm on the  $\text{MnO}_2$  nanosheet (the NPs display clear lattice fringes with a consistent spacing of 0.238 nm, corresponding to the (111) facet of metallic Pd phase).<sup>37</sup> As a comparison, Pd NPs were also deposited over the Ni foam (Pd/Ni foam). The SEM image in Fig. S2a† evidences the larger and aggregated Pd particles (~20 nm) as well as some  $\text{Ni(OH)}_2$  nanosheet assemblies. This structure is also verified by the TEM image of the particle that was scraped from the Pd/Ni foam (Fig. S2b†).

The XRD patterns of the  $\text{MnO}_2$ /Ni foam, Pd/Ni foam, and Pd– $\text{MnO}_2\text{-O}_v$ /Ni foam in Fig. 1g point to the  $\delta$ -form of  $\text{MnO}_2$  (PDFcard #80-1098) and the metallic crystal phase of Pd (PDFcard #05-0681) in all these samples.<sup>38,39</sup> No  $\text{Ni(OH)}_2$  phase is discerned possibly due to its low content. The characteristic diffraction peaks for  $\text{MnO}_2$  become inconspicuous in the Pd– $\text{MnO}_2\text{-O}_v$ /Ni foam, possibly due to the crystallinity reduction of  $\text{MnO}_2$  after the  $\text{O}_v$  introduction or the dense cover of Pd NPs. The ICP analyses reveal that the Pd mass loading on Pd– $\text{MnO}_2\text{-O}_v$ /Ni foam and Pd/Ni foam are similar at 1.6 mg  $\text{cm}^{-3}$ . The presence of  $\text{O}_v$  in the  $\text{MnO}_2\text{-O}_v$ /Ni foam, Pd/Ni foam, and Pd– $\text{MnO}_2\text{-O}_v$ /Ni foam are evidenced by the strong EPR signal at around  $g = 2.0037$  in their spectra (Fig. 1h) as well as the O 1s XPS peak at 530.4 eV (Fig. 1i).<sup>40</sup> The presence of  $\text{O}_v$  on Pd/Ni foam can be ascribed to the involvement of the  $\text{Ni(OH)}_2$  species. Fig. 1i also shows that the Pd– $\text{MnO}_2\text{-O}_v$ /Ni foam carries a larger number of  $\text{O}_v$  than the Pd/Ni foam (35.25% vs. 26.75%), consistent with our speculation that  $\text{O}_v$  is more readily formed on  $\text{MnO}_2$ .

### 3.2. NRR performance

The NRR performances of Pd– $\text{MnO}_2\text{-O}_v$ /Ni foam, Pd/Ni foam, and  $\text{MnO}_2\text{-O}_v$ /Ni foam electrodes were tested and compared. Given the inherent 3D porous structure of the foam, a continuous-flow reaction cell was customized with the effluent penetrating the electrode, as schemed in Fig. 2a, which allows sufficient mass transfer of  $\text{NO}_3^-$ -N around the active sites. Two parallel working electrodes with a distance of 1.0 cm were set to enhance the NRR. Fig. 2b plots the  $C/C_0$  of  $\text{NO}_3^-$ -N in the effluent as a function of electrolysis time under a working potential of  $-0.85$  V, a flow rate of  $0.875$  mL  $\text{min}^{-1}$ , and a feeding  $\text{NO}_3^-$ -N concentration of  $22.5$  mg  $\text{L}^{-1}$ , by which the  $\text{NO}_3^-$ -N conversion efficiency and the rate at the steady state for the electrode can be calculated. As observed, the Pd– $\text{MnO}_2\text{-O}_v$ /Ni foam affords both the largest  $\text{NO}_3^-$ -N conversion efficiency of 90.61% and conversion rate of  $642$  mg  $\text{N m}^{-2}$   $\text{electrode h}^{-1}$ , of which the conversion rate is almost 1.7 and 5.7 times that of the Pd/Ni foam ( $369$  mg  $\text{N m}^{-2}$   $\text{electrode h}^{-1}$ ) and Pd-free  $\text{MnO}_2\text{-O}_v$ /Ni foam ( $118$  mg  $\text{N m}^{-2}$   $\text{electrode h}^{-1}$ ), respectively. As shown by the product distribution in Fig. 2c,  $\text{NH}_3$ -N is the leading product on both the Pd/Ni foam and Pd– $\text{MnO}_2\text{-O}_v$ /Ni foam electrode with a selectivity of 85.02% and 87.64%, respectively, while only a negligible amount of  $\text{NO}_2^-$ -N is tracked (3.72 and 0.25% in product). However, on  $\text{MnO}_2\text{-O}_v$ /Ni foam, only 34.5% of the  $\text{NO}_3^-$  is converted to  $\text{NH}_3$  (another 30.2% to  $\text{NO}_2^-$  and the rest to  $\text{N}_2$ ), which confirms the critical role of Pd in the

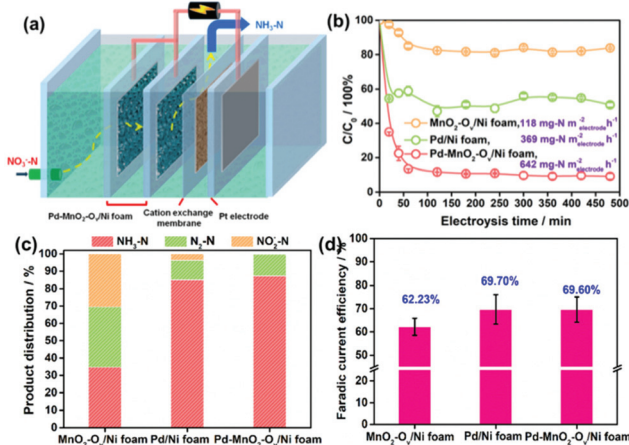
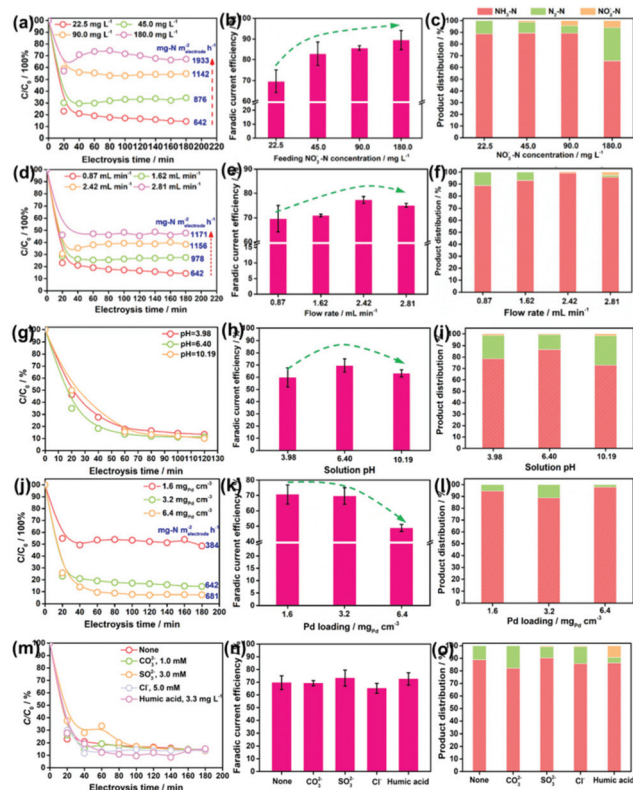


Fig. 2 (a) Schematic description of the sealed continuous-flow reaction cell; (b) plots of  $C/C_0$  as a function of the reaction time; (c) product distribution in the outlet flow at the steady state (note that the present product distribution is an average of the ones determined during the 480 min of NRR in at least three repeated tests, the same below); (d) faradaic current efficiency for the NRR on  $\text{MnO}_2\text{-O}_v$ /Ni foam, Pd/Ni foam, and Pd– $\text{MnO}_2\text{-O}_v$ /Ni foam.

fast and deep reduction of  $\text{NO}_3^-$  to  $\text{NH}_3$ . Here, the  $\text{NH}_3$  is believed to originate from the  $\text{NO}_3^-$  conversion rather than the  $\text{N}_2$  reduction or other impurities in the water as no  $\text{NH}_3$  is detected once the  $\text{NO}_3^-$ -free solution is fed in the flow. Fig. 2d shows that the faradaic current efficiencies for all three electrodes are smaller than 100% due to the side hydrogen evolution reaction (HER). However, the values for the Pd/Ni foam and Pd– $\text{MnO}_2\text{-O}_v$ /Ni foam electrodes are relatively high, approaching 70%.

Impacts of the feeding  $\text{NO}_3^-$ -N concentration, the flowing rate, the solution pH, and the Pd loading on the NRR performances of the Pd– $\text{MnO}_2\text{-O}_v$ /Ni foam electrode were investigated. Fig. 3a evidences the decrease in the  $\text{NO}_3^-$ -N conversion efficiency from 87.06% to 32.87% while the increase in the conversion rate from 642 to 1933 mg  $\text{N m}^{-2}$   $\text{electrode h}^{-1}$  with the feeding  $\text{NO}_3^-$ -N concentration rising from 22.5 to 180.0 mg  $\text{L}^{-1}$ . Fig. 3b shows that the faradaic current efficiency keeps growing with the increment in  $\text{NO}_3^-$ -N concentration and reaches the peak of 89.5% by feeding 180 mg  $\text{L}^{-1}$   $\text{NO}_3^-$ -N. It is therefore suggested that the active sites are more specific to the NRR over HER with more  $\text{NO}_3^-$ -N supplied. The  $\text{NH}_3$  selectivity is kept at a high value of around 90% with 22.5–90.0 mg  $\text{L}^{-1}$   $\text{NO}_3^-$ -N in the influent (Fig. 3c), while it sharply drops to 55.45% with 180.0 mg  $\text{L}^{-1}$   $\text{NO}_3^-$ -N. Correspondingly, the  $\text{N}_2$  yield rises. According to the previous work, the decreased  $\text{NH}_3$  yield and the enhanced  $\text{N}_2$  formation can be attributed to the enlarged N-intermediate/ $\text{H}^*$  ( $\text{N}/\text{H}$ ) ratio on catalyst surface when feeding a larger concentration of  $\text{NO}_3^-$ -N.<sup>41,42</sup>

Fig. 3d reveals that an increase in the flow rate from 0.87 to 2.81 mL  $\text{min}^{-1}$  reduces the  $\text{NO}_3^-$ -N removal efficiency from 87.06% to 52.02%, but raises the  $\text{NO}_3^-$ -N conversion rate from 642 to 1171 mg  $\text{N m}^{-2}$   $\text{electrode h}^{-1}$ . This is rationalized by the



**Fig. 3** Impacts of (a–c) the feeding  $\text{NO}_3^-$ –N concentration, (d–f) flow rate, (g–i) pH, (j–l) Pd loading, and (m–o) co-existing anions and dissolved organics on the  $\text{NO}_3^-$ –N conversion rate, faradaic current efficiency, and product distribution in NRR.

fact that under the larger flow rate, more  $\text{NO}_3^-$  pass by the electrode but stay in a shorter time. Accordingly, a larger proportion of  $\text{NO}_3^-$  incline to flow through the electrode before being reduced, leading to the increased  $\text{NO}_3^-$  residues in the effluent. Despite these, the absolute amount of the converted  $\text{NO}_3^-$ –N is increased as the active sites are feed with more  $\text{NO}_3^-$ –N under the larger flow rate. Fig. 3e and f show that with the increase in flow rate, both the faradaic current efficiency and the  $\text{NH}_3$  selectivity in the product grow, reach the peak at  $2.42 \text{ mL min}^{-1}$  and then decrease. Some  $\text{NO}_2^-$ –N is even detected at  $2.81 \text{ mL min}^{-1}$ . Therefore, it is suggested that the uplift of the flow rate but in a suitable range is conducive to acquire pure  $\text{NH}_3$ –N.

Fig. 3g shows that the solution pH has little effect on both the  $\text{NO}_3^-$ –N conversion rate, faradaic current efficiency, and rate of the electrode. This is beyond expectation as many previous reports have demonstrated that an acidic condition is beneficial to NRR by affording sufficient protons and alleviating the potential poisoning of active sites (e.g.,  $\text{O}_v$  and the Pd sites) by  $\text{OH}^-$ . This inconsistency might be attributed to the overdose of active sites on the electrode when subjected to the low  $\text{NO}_3^-$ –N load, which dilutes the effect of pH. Fig. 3h and i demonstrate that the faradaic current efficiency and the  $\text{NH}_3$  selectivity are maximized at nearly neutral conditions. As observed in Fig. 3i, the

drop in  $\text{NH}_3$  selectivity primarily originates from the increased  $\text{N}_2$  yield. The enhanced  $\text{N}_2$  production in the acidic condition can be ascribed to the formation of  $\text{HNO}_3(\text{aq})$  that readily accumulates and is reduced on the catalyst in comparison to  $\text{NO}_3^-$ ,<sup>43</sup> which contributes to increasing the N/H ratio on electrode, promoting  $\text{N}_2$  formation. The enhanced  $\text{N}_2$  production in the alkaline condition can be attributed to the intensified poisoning of  $\text{O}_v$  by  $\text{OH}^-$  (Fig. S3†). As a result, the NRR primarily occurs on Pd, which, as we know, is one excellent metal to trigger the  $\text{N}_2$  formation.<sup>44</sup>

Fig. 3j reveals that an increment in the Pd loading boosts the  $\text{NO}_3^-$ –N conversion on the electrode under a  $\text{NO}_3^-$ –N feeding concentration of  $22.5 \text{ mg L}^{-1}$ , which further confirms the critical role of Pd in  $\text{NO}_3^-$ –N conversion. Fig. 3k shows that faradaic current efficiency decreases under a larger Pd loading, which results from the enhanced side HER that wastes more electrons. Fig. 3l shows that the moderate Pd loading of  $3.2 \text{ mg}_{\text{Pd}} \text{ cm}^{-3}$  gives rise to the poorest  $\text{NH}_3$  selectivity. As Pd occupies the  $\text{O}_v$  sites during the deposition process, we attribute the higher  $\text{NH}_3$  selectivity at the lower Pd loading to the larger number of  $\text{O}_v$ , which survived at the surface, promoting  $\text{NH}_3$  formation. The higher  $\text{NH}_3$  selectivity at the higher Pd loading is rationalized by the fact that more  $\text{H}^*$  are exported to the  $\text{O}_v$  for  $\text{NO}_3^-$  reduction, and the resultant smaller N/H ratio is conducive to  $\text{NH}_3$  formation.

Given the presence of various anions and dissolved organics in natural water, their impacts on the NRR performances of Pd– $\text{MnO}_2$ – $\text{O}_v$ /Ni foam electrodes have to be considered. The carbonate ( $\text{CO}_3^{2-}$ ,  $1.0 \text{ mM}$ ), sulfite ( $\text{SO}_3^{2-}$ ,  $3.0 \text{ mM}$ ), and chloridion ( $\text{Cl}^-$ ,  $5.0 \text{ mM}$ ) are selected as the probe anions,<sup>45</sup> while the humic acid ( $3.3 \text{ mg L}^{-1}$ ) is selected to represent the dissolved organics.<sup>46</sup> Intriguingly, insignificant differences in the  $\text{NO}_3^-$ –N conversion rate, faradaic current efficiency, and  $\text{NH}_3$  selectivity are observed in Fig. 3m–o after the introduction of anions and humic acid, suggesting the relatively strong resistance of our electrode to the disturbance from natural water environments. The humic acid exhibits some detrimental effects as the  $\text{NO}_2^-$  residues increase to  $9.87\%$ . It hints that a lower organic content in water is conducive to the efficient and complete conversion of  $\text{NO}_3^-$  to  $\text{NH}_3$ .

### 3.3. The dual-site catalysis mechanism

As observed, the Pd– $\text{MnO}_2$ – $\text{O}_v$ /Ni foam delivers both the high  $\text{NO}_3^-$  conversion rate and  $\text{NH}_3$  selectivity, which can be expected by the proposed dual-site reaction mechanism that the  $\text{O}_v$  site adsorbs and activates  $\text{NO}_3^-$  while the Pd site generates  $\text{H}^*$  and exports them to the  $\text{O}_v$  site for NRR. To confirm this mechanism, DFT calculations on the adsorption energy of  $\text{H}^*$ ,  $\text{N}^*$ , and  $\text{O}^*$ , as well as the Gibbs free energy changes for the  $\text{NO}_3^-$  conversion to  $\text{NH}_3$  and  $\text{N}_2$  on  $\text{MnO}_2$ ,  $\text{MnO}_2$ – $\text{O}_v$ , and Pd surfaces, were performed. The  $\delta\text{-MnO}_2$  (001) surfaces without and with one  $\text{O}_v$  are chosen to model fine  $\text{MnO}_2$  and  $\text{MnO}_2$ – $\text{O}_v$ , while Pd (111) is selected as the active Pd surface. Fig. S3† reveals that the  $\text{H}^*$  adsorption on  $\text{MnO}_2$ – $\text{O}_v$  is much weaker than that on Pd, confirming the better performance of Pd in proton harvest (the over-strong H adsorption on fine

$\text{MnO}_2$  can be ascribed to the formation of  $-\text{OH}$  groups. This  $\text{H}^*$  species is inert and cannot be used in NRR. Combining these calculation results with the poor NRR performance of the single  $\text{MnO}_2\text{-O}_v$  in Fig. 2b, we are ascertained that the  $\text{H}^*$  required for NRR is primarily provided by Pd.

Fig. 4a and b compare the Gibbs free energy changes ( $\Delta G$ ) of the elementary reactions occurring during the  $\text{NO}_3^-$  conversion to  $\text{N}_2$  and  $\text{NH}_3$  on  $\text{Pd}(111)$  and  $\text{MnO}_2\text{-O}_v$  (001), respectively. The N-intermediates and elementary reactions are set according to the literature.<sup>14,47,48</sup> Basically, the NRR can be divided into two stages: (I)  $\text{NO}_3^-$  adsorption and its conversion to  $\text{NO}_2^*$ , which is well-known as the rate-determining step of NRR; (II)  $\text{NO}_2^*$  conversion to  $\text{N}_2$  or  $\text{NH}_3$ , which is considered as the determinant of product selectivity. As observed, the process I on the  $\text{MnO}_2\text{-O}_v$  surface is spontaneous with an overall negative  $\Delta G$  of  $-3.56$  eV, while that on the Pd surface has to overcome an energy barrier of  $0.51$  eV ( $0.48$  eV for  $\text{NO}_3^-$  adsorption and  $0.03$  eV for  $\text{NO}_3^*$  hydrogenation). More intriguingly,  $\text{O}_v$  is found to have the ability to grab one O atom from both  $\text{NO}_3^*$  and  $\text{NO}_2^*$  and complete the  $\text{NO}_3^*-\text{NO}^*$  conversion along with their adsorption processes. All these calculation results clearly verify that  $\text{NO}_3^-$  is preferred to be adsorbed and activated on  $\text{MnO}_2\text{-O}_v$  rather than the Pd site. It should be mentioned that  $\text{O}_v$  is filled by the oxygen atoms during the  $\text{NO}_3^-/\text{NO}_2^*$  activation and should be regenerated under the synergy of polarization potential and  $\text{H}^*$  by overcoming an energy barrier of  $0.87$  eV ( $(1.23-0.36)$  eV).

In stage II, the  $\text{NO}^*$  on  $\text{MnO}_2\text{-O}_v$  is ready to be deeply hydrogenated to  $\text{NH}_3^*$  in an energetically favored pathway of  $\text{NO}^* \rightarrow \text{NOH}^* \rightarrow \text{N}^* \rightarrow \text{NH}^* \rightarrow \text{NH}_2^* \rightarrow \text{NH}_3^*$  with the  $\Delta G$  of all the steps displaying negative values. The  $\text{N}_2$  formation is relatively difficult as the  $\text{N}^*-\text{N}^*$  pairing requires extra energy of  $0.43$  eV. In comparison, the  $\text{NO}_2^*$  conversion to  $\text{NH}_3$  and  $\text{N}_2$  on  $\text{Pd}(111)$  experiences similar energy profiles, pointing to the rela-

tively poor product selectivity to  $\text{NH}_3$  or  $\text{N}_2$  on the Pd site. This is consistent with the previous reports that a mixed product of  $\text{NH}_3$  and  $\text{N}_2$  can be formed on Pd-based catalysts.<sup>49,50</sup> Combining the calculation results with the high  $\text{NH}_3$  selectivity of  $\text{Pd-MnO}_2\text{-O}_v$  in Fig. 2c, we are ascertained that the  $\text{O}_v$  site is the active center for the selective conversion of  $\text{NO}_3^-$  to  $\text{NH}_3$ .

We also examined the adsorption energies of  $\text{N}^*$  and  $\text{O}^*$  on  $\text{MnO}_2\text{-O}_v$  and Pd, and the results in Fig. 4c and d reveal the much stronger adsorption of  $\text{O}^*$  and  $\text{N}^*$  on the  $\text{O}_v$  site of  $\text{MnO}_2\text{-O}_v$  than that on Pd. Given the linear scale of the adsorption energies for N-intermediates with that for either an oxygen or nitrogen atom,<sup>51,52</sup> all the N-intermediates are believed to be preferably immobilized and reduced at the  $\text{O}_v$  site during NRR, which reduces their encountering possibilities and contributes to high  $\text{NH}_3$  selectivity.

On the basis of all the above, we firmly believe the dual-site NRR mechanism on  $\text{MnO}_2\text{-O}_v\text{-Pd}$ , which is schematically described in Fig. 4e. The  $\text{O}_v$  serves to adsorb, immobilize, and activate the  $\text{NO}_3^-$  and N-intermediates, while Pd supplies the  $\text{O}_v$  with sufficient  $\text{H}^*$  for both the NRR and  $\text{O}_v$  refreshment. Such a dual-site NRR mechanism accounts for both the efficient NRR and the high  $\text{NH}_3$  selectivity.

## 4. Conclusions

This work demonstrates the superior performance of the three-dimensional porous  $\text{Pd-MnO}_2\text{-O}_v\text{/Ni}$  foam electrode for NRR. In a continuous-flow reaction cell, it delivers a substantial  $\text{NO}_3^-$ -N conversion rate of  $642 \text{ mg N m}^{-2} \text{ electrode h}^{-1}$  and a  $\text{NH}_3$  selectivity of  $87.64\%$  under  $-0.85$  V when feeding a  $22.5 \text{ mg L}^{-1} \text{ NO}_3^-$ -N solution at a rate of  $0.875 \text{ mL min}^{-1}$ , outperforming the  $\text{Pd/Ni}$  foam ( $369 \text{ mg N m}^{-2} \text{ electrode h}^{-1}$ ,  $84.02\%$ ) and  $\text{MnO}_2\text{-O}_v\text{/Ni}$  foam ( $118 \text{ mg N m}^{-2} \text{ electrode h}^{-1}$ ,  $32.25\%$ ). Combining the experimental characterizations and the theoretical calculations, we confirm the dual-site NRR process on  $\text{Pd-MnO}_2\text{-O}_v$ , in which the  $\text{MnO}_2\text{-O}_v$  serves to adsorb, immobilize, and activate the  $\text{NO}_3^-$  and the N-intermediates, while Pd supplies the  $\text{O}_v$  with sufficient  $\text{H}^*$  for both the NRR and  $\text{O}_v$  refreshment. This work highlights the critical role of dual-site catalysis in the efficient and selective nitrate conversion to  $\text{NH}_3$ , paving the way for utilizing dual-site catalysis in both the nitrate pollution abatement and nitrogen resource recycling from nitrate wastewater.

## Conflicts of interest

The authors declare no competing financial interest.

## Acknowledgements

We acknowledge the funding support from the National Natural Science Foundation of China (2217061059 and 51978110), the Program for the Top Young Talents of

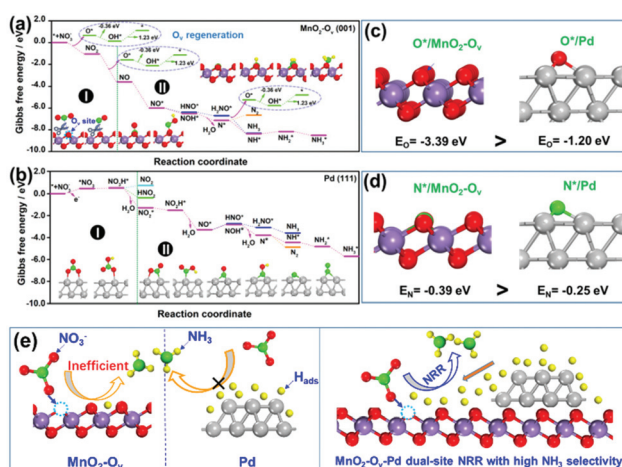


Fig. 4 The reaction energy diagram for the conversion of  $\text{NO}_3^-$  to  $\text{N}_2$  and  $\text{NH}_3$  over (a) clean  $\text{MnO}_2\text{-O}_v$  (001) and (b)  $\text{Pd}(111)$  facet; adsorption energies of (c) one oxygen atom and (d) one nitrogen atom on  $\text{MnO}_2\text{-O}_v$  (001) and  $\text{Pd}(111)$  facets; (e) schematic illustration of the  $\text{MnO}_2\text{-O}_v\text{-Pd}$  dual-site NRR mechanism for a high  $\text{NH}_3$  selectivity.

Chongqing, Innovation group of new technologies for industrial pollution control of Chongqing Education Commission (CXQT19023), and Science and Technology Research Program of Chongqing Municipal Education Commission (KJQN201800829 and KJZD-K202000802).

## Notes and references

- 1 L. Liu, X. Zhang, W. Xu, X. Liu, Y. Li, J. Wei, M. Gao, J. Bi, X. Lu, Z. Wang and X. Wu, *J. Agric. Food Chem.*, 2020, **68**, 3354–3361.
- 2 F. Jiao and B. Xu, *Adv. Mater.*, 2019, **31**, 1805173.
- 3 N. Lazouski, M. Chung, K. Williams, M. L. Gala and K. Manthiram, *Nat. Catal.*, 2020, **3**, 463–469.
- 4 Y. Zhao, L. Zheng, R. Shi, S. Zhang, X. Bian, F. Wu, X. Cao, G. I. N. Waterhouse and T. Zhang, *Adv. Energy Mater.*, 2020, **10**, 2002199.
- 5 M. C. Kim, H. Nam, J. Choi, H. S. Kim, H. W. Lee, D. Kim, J. Kong, S. S. Han, S. Y. Lee and H. S. Park, *ACS Catal.*, 2010, **10**, 10577–10584.
- 6 G. M. Jiang, X. W. Li, M. N. Lan, T. Shen, X. S. Lv, F. Dong and S. Zhang, *Appl. Catal., B*, 2017, **205**, 532–540.
- 7 Y. Zeng, C. Priest, G. Wang and G. Wu, *Small Methods*, 2020, **4**, 2000672.
- 8 Y. T. Wang, Y. F. Yu, R. R. Jia, C. Zhang and B. Zhang, *Natl. Sci. Rev.*, 2019, **6**, 730–738.
- 9 X. Fu, X. Zhao, X. Hu, K. He, Y. Yu, T. Li, Q. Tu, X. Qian, Q. Yue, M. R. Wasielewski and Y. Kang, *Appl. Mater. Today*, 2020, **19**, 100620.
- 10 C. Yu, X. Huang, H. Chen, H. C. J. Godfray, J. S. Wright, J. W. Hall, P. Gong, S. Ni, S. Qiao, G. Huang, Y. Xiao, J. Zhang, Z. Feng, X. Ju, P. Ciais and N. C. Stenseth, *Nature*, 2019, **567**, 516–520.
- 11 S. Wang, X. Zhang, C. Wang, X. Zhang, S. Reis, J. Xu and B. Gu, *Sci. Data*, 2020, **7**, 379.
- 12 J. Wang, T. Feng, J. Chen, V. Ramalingam, Z. Li, D. M. Kabtamu, J. H. He and X. Fang, *Nano Energy*, 2021, **86**, 106088.
- 13 T. Zhu, Q. Chen, P. Liao, W. Duan, S. Liang, Z. Yan and C. Feng, *Small*, 2020, **16**, 2004526.
- 14 X. D. Wang, M. Q. Zhu, G. S. Zeng, X. Liu, C. Fang and C. H. Li, *Nanoscale*, 2020, **12**, 9385–9391.
- 15 X. Chen, T. Zhang, M. Kan, D. Song, J. Jia, Y. Zhao and X. Qian, *Environ. Sci. Technol.*, 2020, **54**, 13344–13353.
- 16 Y. T. Wang, W. Zhou, R. R. Jia, Y. F. Yu and B. Zhang, *Angew. Chem., Int. Ed.*, 2020, **59**, 5350–5354.
- 17 R. R. Jia, Y. T. Wang, C. H. Wang, Y. F. Ling, Y. F. Yu and B. Zhang, *ACS Catal.*, 2020, **10**, 3533–3540.
- 18 H. Hirakawa, M. Hashimoto, Y. Shiraishi and T. Hirai, *J. Am. Chem. Soc.*, 2017, **139**, 10929–10936.
- 19 D. A. Tompsett, S. C. Parker and M. S. Islam, *J. Am. Chem. Soc.*, 2014, **136**, 1418–1426.
- 20 J. Liu, Y. Wei, P.-Z. Li, P. Zhang, W. Su, Y. Sun, R. Zou and Y. Zhao, *ACS Catal.*, 2018, **8**, 3865–3874.
- 21 G. Zhu, J. Zhu, W. Li, W. Yao, R. Zong, Y. Zhu and Q. Zhang, *Environ. Sci. Technol.*, 2018, **52**, 8684–8692.
- 22 M. Zang, N. Xu, G. Cao, Z. Chen, J. Cui, L. Gan, H. Dai, X. Yang and P. Wang, *ACS Catal.*, 2018, **8**, 5062–5069.
- 23 T. Zheng, W. Sang, Z. He, Q. Wei, B. Chen, H. Li, C. Cao, R. Huang, X. Yan, B. Pan, S. Zhou and J. Zeng, *Nano Lett.*, 2017, **17**, 7968–7973.
- 24 Y. Y. Peng, M. Y. Cui, Z. Y. Zhang, S. Shu, X. L. Shi, J. T. Brosnahan, C. Liu, Y. L. Zhang, P. Godbold, X. M. Zhang, F. Dong, G. M. Jiang and S. Zhang, *ACS Catal.*, 2019, **9**, 10803–10811.
- 25 W. Yu, H. Jiang, J. Fang and S. Song, *Environ. Sci. Technol.*, 2021, **55**, 10087–10096.
- 26 X. Li, X. Huang, S. Xi, S. Miao, J. Ding, W. Cai, S. Liu, X. Yang, H. Yang, J. Gao, J. Wang, Y. Huang, T. Zhang and B. Liu, *J. Am. Chem. Soc.*, 2018, **140**, 12469–12475.
- 27 S. Campisi, C. E. Chan-Thaw, L. E. Chinchilla, A. Chutia, G. A. Botton, K. M. H. Mohammed, N. Dimitratos, P. P. Wells and A. Villa, *ACS Catal.*, 2020, **10**, 5483–5492.
- 28 N. Liu, M. Xu, Y. Yang, S. Zhang, J. Zhang, W. Wang, L. Zheng, S. Hong and M. Wei, *ACS Catal.*, 2019, **9**, 2707–2717.
- 29 W. Duan, G. Li, Z. Lei, T. Zhu, Y. Xue, C. Wei and C. Feng, *Water Res.*, 2019, **161**, 126–135.
- 30 G. Kresse and J. Furthmüller, *Phys. Rev. B: Condens. Matter Mater. Phys.*, 1996, **54**, 11169–11186.
- 31 J. P. Perdew, K. Burke and M. Ernzerhof, *Phys. Rev. Lett.*, 1996, **77**, 3865–3868.
- 32 D. R. Hamann, M. Schlüter and C. Chiang, *Phys. Rev. Lett.*, 1979, **43**, 1494–1497.
- 33 X. Guo, J. Gu, S. Lin, S. Zhang, Z. Chen and S. Huang, *J. Am. Chem. Soc.*, 2020, **142**, 5709–5721.
- 34 J. H. Montoya, C. Tsai, A. Vojvodic and J. K. Nørskov, *ChemSusChem*, 2015, **8**, 2180–2186.
- 35 S. Grimme, *J. Comput. Chem.*, 2006, **27**, 1787–1799.
- 36 M. Bajdich, M. Garcia-Mota, A. Vojvodic, J. K. Nørskov and A. T. Bell, *J. Am. Chem. Soc.*, 2013, **135**, 13521–13530.
- 37 G. M. Jiang, X. J. Li, Y. Shen, X. L. Shi, X. S. Lv, X. M. Zhang, F. Dong, G. X. Qi and R. Liu, *J. Catal.*, 2020, **391**, 414–423.
- 38 X. Fang, Y. Liu, W. Cen and Y. Cheng, *Ind. Eng. Chem. Res.*, 2020, **59**, 14606–14615.
- 39 W. Yang, Y. Zhu, F. You, L. Yan, Y. Ma, C. Lu, P. Gao, Q. Hao and W. Li, *Appl. Catal., B*, 2018, **233**, 184–193.
- 40 J. Wang, J. G. Wang, X. Qin, Y. Wang, Z. You, H. Liu and M. Shao, *ACS Appl. Mater. Interfaces*, 2020, **12**, 34949–34958.
- 41 S. Hamid, M. A. Kumar and W. Lee, *Appl. Catal., B*, 2016, **187**, 37–46.
- 42 P. J. Kuang, K. Natsui and Y. Einaga, *Chemosphere*, 2018, **210**, 524–530.
- 43 C. A. Clark, C. P. Reddy, H. Xu, K. N. Heck, G. H. Luo, T. P. Senftle and M. S. Wong, *ACS Catal.*, 2019, 494–509.
- 44 H. Shin, S. Jung, S. Bae, W. Lee and H. Kim, *Environ. Sci. Technol.*, 2014, **48**, 12768–12774.

45 Y. M. Kang, M. K. Kim and K. D. Zoh, *Chemosphere*, 2018, **204**, 148–155.

46 B. P. Chaplin, E. Roundy, K. A. Guy, J. R. Shapley and C. J. Werth, *Environ. Sci. Technol.*, 2006, **40**, 3075–3081.

47 R. Jia, Y. Wang, C. Wang, Y. Ling, Y. Yu and B. Zhang, *ACS Catal.*, 2020, **10**, 3533–3540.

48 J. Long, S. M. Chen, Y. L. Zhang, C. X. Guo, X. Y. Fu, D. H. Deng and J. P. Xiao, *Angew. Chem., Int. Ed.*, 2020, **59**, 9711–9718.

49 H. Li, S. J. Guo, K. Shin, M. S. Wong and G. Henkelman, *ACS Catal.*, 2019, **9**, 7957–7966.

50 P. Gayen, J. Spataro, S. Avasarala, A. M. Ali, J. M. Cerrato and B. P. Chaplin, *Environ. Sci. Technol.*, 2018, **52**, 9370–9379.

51 J. X. Liu, D. Richards, N. Singh and B. R. Goldsmith, *ACS Catal.*, 2019, **9**, 7052–7064.

52 J. P. Troutman, H. Li, A. M. Haddix, B. A. Kienzle, G. Henkelman, S. M. Humphrey and C. J. Werth, *ACS Catal.*, 2020, **10**, 7979–7989.